basal firn layer, coupled to removal of gases by vertical advection of air caused by compression of the firn. The effusional enrichment ratio for two isotopes is controlled by the kinetic fractionation factor $\alpha = (M/M_j)^{1/2}$, and the resulting isotope enrichment is given by the Rayleigh equation:

$$R/R_0 = (1 - F_L)^{\alpha - 1}$$

where F_L is the fraction of component N lost by effusion through a molecular leak. Because effusional enrichment depends on the fractional gas loss, the expected gravitational and effusional enrichments cannot be compared unless F_L is specified. We used the mean $^{18}O/^{16}O$ enrichment in the ice samples to calculate a fictive value of 1.79% for $F_L(O_2)$ and then scaled the F_L values for other components to $F_L(O_2)$. Thus, $[1 - F_L(j)] = [1 - F_L(O_2)]^{\alpha(j)}$, where $\alpha(j) = (M_{O_2}/M_j)^{1/2}$, the fractionation factor for any component j versus O_2. The resulting F_L values (1.91% for N_2 and 1.69% for ^{36}Ar) were then used to calculate the other effusional ratio enrichments, scaled to $F_L(O_2)$. The effusional and gravitational enrichments ($Z = 60$ m, $T = -20°C$) for the various ratios are as follows:

Component	Δ(Eff) per mil)	Δ(Grav) per mil)
$\delta^{15}N$	0.33	0.28
$\delta^{18}O$	0.54	0.56
$\delta^{40}Ar$	0.87	1.12
$\Delta(O_2/N_2)$	1.24	1.11
$\Delta(Ar/N_2)$	3.14	3.35
$\Delta(^{84}Kr/^{36}Ar)$	5.90	13.50
$\Delta(^{132}Xe/^{36}Ar)$	8.18	26.85

The gravitational and effusional ratio enrichments are indistinguishable within limits of analytical accuracy for all these ratios, with the exception of the $^{84}Kr/^{36}Ar$ and $^{132}Xe/^{36}Ar$ pairs, for which the gravitational enrichments are 2.3 and 3.3 times the calculated effusional effects, respectively. Moreover, the predicted ratio of $^{84}Kr/^{36}Ar$ to $^{18}O/^{16}O$ enrichments is 24.1 for gravitational separation versus only 10.9 for effusion. Note that the effusional enrichment ratio is constant over the range of Fig. 2 because, to first order, the ratio is simply $\alpha(36/32)[\alpha(84/36) - 1]/[\alpha(34/32) - 1] = 10.9$. (Here, the mass numbers are used only as labels for the individual fractionation factors.)

7. See H. Craig, K. Marti, R. Wiens, *A Static Mass Spectrometer with Triple Collection for Nitrogen and Neon Isotopes* (Scripps Institution of Oceanography Tech. Rep. 93-11, 1993) for details of the Kr/Ar ratio analyses. Gases trapped in bubbles were extracted by melting ice samples (~30 g) in a high-vacuum system, after which aliquots were taken for various analyses. For the noble gas measurements, sample analyses were alternated with measurements on the on-line machine air standard, and all measurements were made at the same ^{36}Ar ion beam intensity. Three samples of air were put through the extraction procedures and analyzed with the ice samples; Table 1 shows that the observed ratios were indistinguishable from the machine air standard. The stable isotope ratios were measured on a 10-inch-radius, triple-collection mass spectrometer (SAMSON). The gases were cycled over a hot carbon filament to convert O_2 to CO_2 for the mass spectrometer, and the remaining N_2-Ar fraction was introduced into the spectrometer through I_2O_5 reagent to remove all traces of CO. The Ar/N_2 ratios were measured by conventional gas chromatography (GC); although these ratios are accurate to only ~5 per mil in our GC system, they are important because it was previously shown (2) that large negative enrichments in both Ar/N_2 and O_2/N_2 can be caused by loss of gases from ice through microfractures, due to differential capillary effects during pumping. The measured Ar/N_2 ratios are consistent with enrichments expected for either gravitational or effusional fractionation and show no significant effect of possible gas loss.
8. H. Craig, *Science* **159**, 93 (1968).
9. R. F. Weiss, *Deep-Sea Res.* **17**, 721 (1970); *J. Chem. Eng. Data* **16**, 235 (1971); D. Wood and R. Caputi, *U.S. Naval Radiol. Defense Lab. Tech. Pub. USNRDL-TR-988* (1966).
10. M. Stute, P. Schlosser, J. F. Clark, W. S. Broecker,

Science **256**, 1000 (1992). The 5°C global cooling during the last glacial maximum is based on the noble gas geothermometer (using Ne, Kr, and Xe) for ground water. (The temperatures obtained by this method need corrections for the solubility effects on atmospheric partial pressures.)
11. K. M. Cuffey *et al., Science* **270**, 455 (1995). The −52°C temperature estimate for central Greenland is based on fitting ice-core ^{18}O data to a borehole temperature model.
12. We thank J. Welhan and the members of the PICO group for drilling the Dye 3 ice core, D. Burtner for laboratory assistance, K. Turekian for discussion, and C. C. Langway Jr. for his interest in and enthusiasm for our ice-core work. R. Keeling pointed out to us that atmospheric concentrations will be affected by global temperature changes. Supported by the Polar Programs Office of NSF.

River Meandering as a Self-Organization Process

Hans-Henrik Stølum

Simulations of freely meandering rivers and empirical data show that the meandering process self-organizes the river morphology, or planform, into a critical state characterized by fractal geometry. The meandering process oscillates in space and time between a state in which the river planform is ordered and one in which it is chaotic. Clusters of river cutoffs tend to cause a transition between these two states and to force the system into stationary fluctuations around the critical state.

The meandering river system is characterized by recurrent river planform patterns, repeated with little variation from one river to the next irrespective of their magnitude and from one scale to another within each river. This consistency suggests that a higher level of processes forms by self-organization from the physical processes of deposition and erosion operating in the system. These physical processes may be described by continuum fluid mechanics. Although meandering dynamics can be simulated from models based on continuum mechanics, such models reveal little about the holistic, spatiotemporal properties of the meandering process, for example, the hierarchical, fractal geometry of the river planform. [Self-affine fractal scaling of meandering river planforms was first suggested in (1) and has been analyzed in (2, 3).] It has therefore been suggested that meandering needs to be understood in terms of chaotic dynamics and self-organization (4–6). In this report, I use a fluid mechanical model developed by Parker, Howard, and co-workers (7, 8) to explore the dynamical properties of meandering by simulation.

Meandering is caused by the operation of two opposing processes (4), which are linked by a complex feedback that is partly under local geometrical control: lateral migration acts to increase sinuosity, whereas cutoffs (the formation of oxbow lakes) act to decrease it. Lateral migration results from bend erosion and deposition (4, 9). Cutoffs arise from a local geometry (Kinoshita shape), which is created by the lateral migration process (4, 10, 11).

The state of the system is conveniently measured by the dimensionless parameter sinuosity

$$s = L/\ell$$

where L is the length of the river along its course between two points and ℓ is the shortest length between the same points. The quantities L and ℓ are measured in units of average width, w. When the river is straight, sinuosity has a minimum value of 1. In principle, no maximum value exists. Sinuosity is related to the information content and symmetry of the system (5). Oxbow lakes have a finite length range, with a minimum value of ≈ 7 and a maximum of $\approx 40w$.

In the simulations (Fig. 1, A and B), the river typically formed two coexisting domains, one with consistently high sinuosity (mean $s \approx 3.5$) and one with consistently low sinuosity (mean $s \approx 2.7$). Because a straight line is the most ordered state the river can take (zero entropy, perfect axial symmetry), the low-sinuosity regions represent a distinctly more ordered state than the high-sinuosity regions (weak versus strong asymmetry).

The low-sinuosity domains in Fig. 1, A and B, formed as a result of a clustering of cutoff events. Each cutoff has a tendency to trigger other cutoffs in its vicinity by causing accelerated local change, and this may generate a cluster of cutoffs in space and time. Similarly, in natural rivers, successive cutoffs occur only rarely with the same spacing or at regular intervals, and so clusters are formed.

When the simulated river was locally straightened by cutoffs, the dynamics died down to create a window of slow change that persisted for awhile, before a gradual

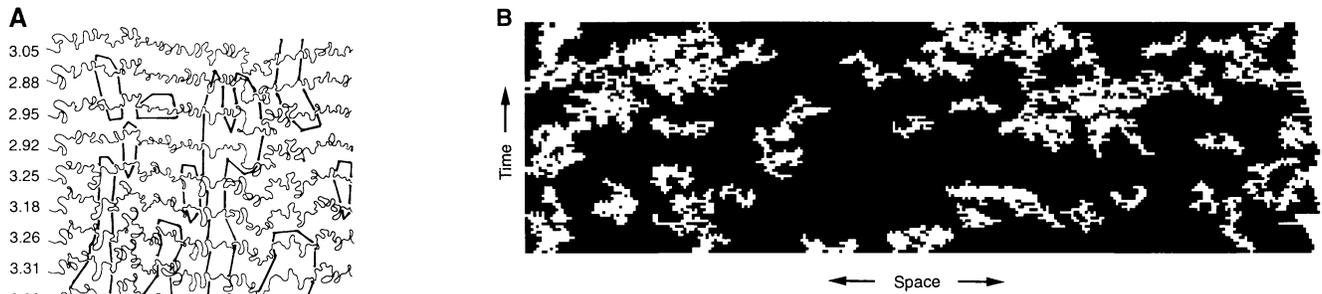Department of Earth Sciences, University of Cambridge, Cambridge CB2 3EQ, UK.

Fig. 1. (A) The spatiotemporal evolution of a river during a period of 4000 iterations. Mean river length is 1570w. The state of the river planform was recorded every 200 iterations, and a simple tracking routine was used to find segments of sinuosity above or below a value of 3.14 and longer than 30 river width units. This yielded a pattern of intermittent domains of an ordered (low-sinuosity) state with mean sinuosity of ≈2.4 (encircled). These domains coexist with a chaotic state having a mean sinuosity of ≈3.5. Numbers at the left refer to the total sinuosity of each river planform. (See Fig. 3A for further details of the simulation run.) **(B)** The evolution of local sinuosity ($\ell = 3w$) in space and time shows the full-scale range of low-sinuosity domains of intermittent order (white). The black background is the chaotic (high-sinuosity) state. The time interval spans 16,000 iterations with every 200 iterations shown [this interval is located within a regime of stationary global sinuosity, as is that of (A)]. Mean river length is 3000w.

buildup of sinuosity. Such low-sinuosity domains are intermittent windows of relative order in the chaotic high-sinuosity state (5, 12). Within this state, change is rapid and the system has little capacity for retaining spatial information (hardly any single meander persisted in recognizable form for more than ≈400 iterations).

The effect of cutoffs depends on the state of the system. Cutoffs in the chaotic state are likely to bring the system over to the ordered state (Figs. 1A, 1B, and 2C), whereas cutoffs in the (mature) ordered state are likely to bring about chaos (Fig. 2A). The immediate effect of cutoffs is always to lower sinuosity, but their long-term effect is context-dependent. In the ordered state, cutoffs tend to induce strong axial asymmetries (create sharp bends), which are subsequently amplified by the meandering process (Fig. 2B). In the chaotic state, cutoffs tend to remove the most asymmetric parts of the river (large and often irregular Kinoshita meanders), causing the system to revert back to a state with weak axial and bend asymmetries (Fig. 2C).

In the simulations, an increase in sinuosity is caused by the slow enlargement of river bends that is in turn caused by bank erosion (Fig. 2B). A decrease in sinuosity is caused by cutoff events (Fig. 2C). These opposing processes self-organize the sinuosity into a steady state around a mean value of $s = 3.14$, the sinuosity of a circle (π) (13, 14) (Fig. 3A). The mean value of π follows from the fractal geometry of the planform (14). This is the intermediate sinuosity value characterizing the transitions between domains of the two states seen in Fig. 1, A
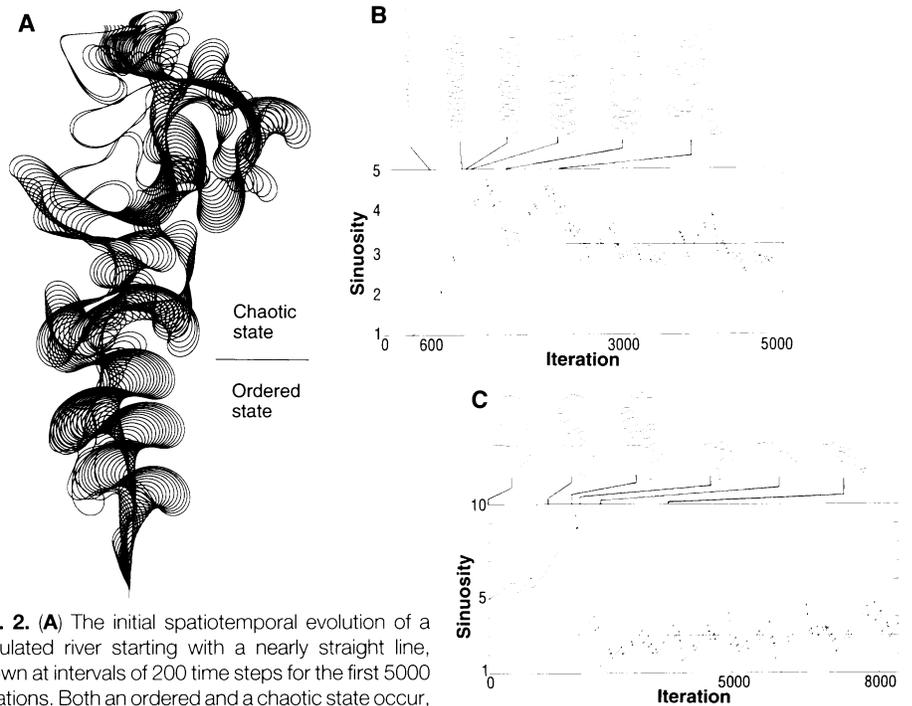

Fig. 2. (A) The initial spatiotemporal evolution of a simulated river starting with a nearly straight line, shown at intervals of 200 time steps for the first 5000 iterations. Both an ordered and a chaotic state occur, with the transition between them initiated by a cutoff cluster. The ordered state in the lower part of the figure has reached a mature stage in which the train of bends is still highly symmetrical around the original axis, while at the same time each bend is growing into an asymmetrical shape (Kinoshita shape) (11). The chaotic state seen in the upper half of the figure was initiated by a cutoff cluster occurring in the ordered state. **(B)** The spatiotemporal self-organization process during the initial part of the time series in Fig. 3A (starting from a nearly straight path). After an initial growth phase due to development of a wave form with increasing amplitude, the sinuosity falls off in steps as neighboring bends grow to meet each other, causing a series of cutoffs. **(C)** Spatiotemporal self-organization when starting from an arbitrarily curved initial path with sinuosity $s = 5.0$. As in (B) there is an initial rapid growth phase as undulations begin to grow on the original convolutions, followed by two anomalously large cutoff events that bring the sinuosity down to ≈1.3.

and B. That the steady state originates from two opposing processes is confirmed by the monotonic rise in sinuosity when the cutoff process is suppressed (Fig. 3B). Figure 2, B and C, demonstrates that sinuosity will go to a stationary state around the same aver-

age sinuosity (π) independently of initial conditions. This robustness of the self-organization process suggests a dynamical state of self-organized criticality (SOC) (4, 6).

If the simulated river actually goes to SOC, then spatial and temporal power-law

scaling would be expected (6). The SOC model predicts that the cutoff (oxbow lake) clusters correspond to the dynamical notion of "avalanches" with a fractal size distribution. This idea is confirmed by the total distribution of single and clustered oxbow lakes [using a clustering criterion (15)], which follows a power law over nearly two orders of magnitude (Fig. 4A). I analyzed the scaling properties of sinuosity fluctuations in the stationary state by rescaled range (R/S) analysis, which is a method for identifying power-law scaling in time series (16). The R/S analysis detected power-law scaling over

two orders of magnitude (Fig. 4B), an indication that the fluctuations are invariant with respect to scale. Finally, the SOC state is associated with power-law scaling in space. The bends of the simulated river scale over more than two orders of magnitude, with a fractal dimension close to the dimension measured for the freely meandering Juruá River, Brazil (Fig. 4C) (3, 17, 18).

In river meandering simulations, the dynamical state of SOC is related to the occurrence of spatiotemporal chaos and intermittency as follows: In the ordered state cutoffs act to destroy order, whereas in the disor-

dered (chaotic) state cutoffs create order. Each cutoff also increases the probability of cutoff formation in its vicinity by accelerating local change, thereby giving rise to spatiotemporal clusters (avalanches) of cutoffs. This avalanche dynamics is an equalizer that keeps the system fluctuating around a critical state, by creating and extinguishing coexisting domains of order and chaos. The simulated meandering river is therefore in a state of eternal recurrence (19).

REFERENCES AND NOTES

1. B. B. Mandelbrot, *The Fractal Geometry of Nature* (Freeman, New York, 1983).
2. R. S. Snow, *Pure Appl. Geophys.* **131**, 99 (1989).
3. H.-H. Stølum, *Geol. Soc. Am. Bull.*, in press.
4. D. Furbish, *ibid.* **103**, 1576 (1991); H.-H. Stølum, *Am. Assoc. Pet. Geol. Bull.* **75**, 677 (abstr.) (1991); K. Montgomery, *Area* **25**, 98 (1993). "Chaos" is a form of deterministic motion that is sensitively dependent on initial conditions. This causes rapid changes and short "memory" within the system. However, short-lived intervals of regularity or order (intermittency) commonly arise sporadically in chaos (5). Montgomery (cited above) demonstrated that the meandering river behaves as a weakly chaotic dynamical system with small positive Lyapunov exponents. Small Lyapunov exponents are characteristic of intermittent chaos when the ordered and chaotic domains are not measured separately. "Self-organized criticality" refers to a tendency of dissipative systems to reach a state of stationary fluctuations around a critical state independently of initial conditions. The fluctuations are driven by a process of discrete events clustered in time and space ("avalanches"), which gives rise to a fractal (scale-invariant or -covariant) structure in time and space (6).
5. F. C. Hoppensteadt, *Analysis and Simulation of Chaotic Systems* (Springer, New York, 1993); H.-W. Lorentz, *Nonlinear Dynamical Economics and Chaotic Motion* (Springer, Berlin, ed. 2, 1993).
6. P. Bak, C. Tang, K. Wiesenfeld, *Phys. Rev. Lett.* **59**, 381 (1987); M. Paczuski and P. Bak, *Phys. Rev.* **48**, R3214 (1993); S. Maslov, M. Paczuski, P. Bak, *Phys. Rev. Lett.* **73**, 2162 (1994); S. Boettcher and M. Paczuski, *Phys. Rev. Lett.* **76**, 348 (1996).
7. A. D. Howard and T. R. Knutson, *Water Resour. Res.* **20**, 1656 (1984); A. D. Howard, in *River Meandering*, C. M. Elliott, Ed. (American Society of Civil Engineers, New York, 1984), pp. 952–963; A. D. Howard and A. T. Hemberger, *Geomorphology* **4**, 161 (1991); A. D. Howard, in *Lowland Floodplain Rivers*, P. A. Carling and G. E. Petts, Eds. (Wiley, Chichester, UK, 1992), pp. 1–40.
8. The simulator is based on a fluid mechanical model of river flow developed by G. Parker and E. D. Andrews [*J. Fluid Mech.* **162**, 139 (1986)], S. Ikeda, G. Parker, and K. Sawai [*ibid.* **112**, 363 (1981)], and H. Johannesen and G. Parker [in *River Meandering*, S. Ikeda and G. Parker, Eds. (American Geophysical Union, Water Research Monograph, vol. 12, Washington, DC, 1989), pp. 379–415]. This is a simplified mechanistic model of bend evolution. The treatments of both bend extension and cutoff involve substantial approximations. Still, in terms of scaling pattern, the bend trains predicted by the model are statistically indistinguishable from real bend trains [see (3) and the comparison in Fig. 4C]. Therefore, the model appears to be a reasonable first-order representation of meandering dynamics. The subtle statistical difference between simulations and rivers found by Howard and Hemberger [see (7)] was based on an earlier version of the simulator that did not incorporate the results of Johannesen and Parker. The model does not take into account chute cutoffs (which largely occur during high flood stages) (10). The simuations therefore model rivers with discharge fluctuations that are small enough so that chute cutoffs are rare or do not occur. Further, the simulations represent free meandering—that is, meandering on a sloping plane rather than in a confining valley. These limitations are reasonable ap-
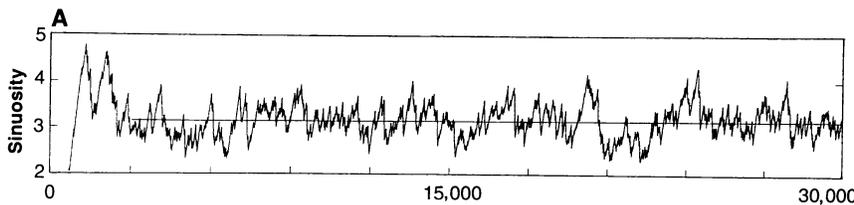
Fig. 3. (**A**) Time series of sinuosity evolution from the simulation of a free meandering river with constant discharge and uniform bank resistance at low gradient corresponding to $b = 2$. The initial state is a quasistraight course ($\ell = 500w$) with random perturbations and $s \approx 1$. The straight line in the stationary part of the time series is the mean sinuosity of 3.14 ± 0.34 (13). (**B**) Enlargement of the initial part of the time series in (A), compared to the evolution of sinuosity if the cutoff process does not occur.
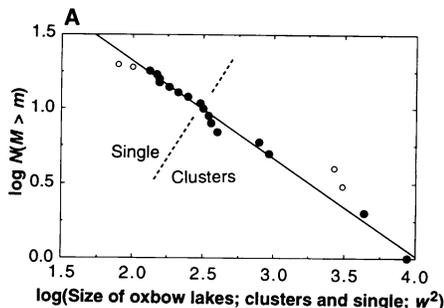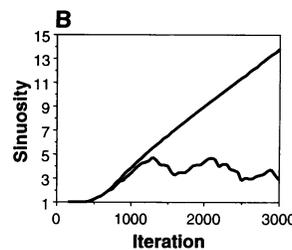

Fig. 4. (**A**) Cumulative size-frequency distribution of oxbow lakes generated by the simulation described in Fig. 1B. The distribution includes oxbow lake clusters [generated according to a simple clustering criterion (15)] and the residual single oxbow lakes. The straight line is a fit of the function $N(M > m) = 2.64m^{-0.66}$ to 16 of 20 avalanches (filled circles), where $N(M > m)$ is the number of avalanches larger than size m (area enclosed by an avalanche). Deposition rate was chosen as 0.024 width units per iteration. This is the smallest value that does not generate overlapping sand-bodies (for a sandbody thickness of $3w$) and at the same time gives a total depth roughly equal to the length of section. The depth and length thresholds could then be set as equal. The value used, $26.3w$, is close to the percolation threshold in the depth direction ($26.7w$). (**B**) The R/S analysis of the sinuosity time series of Fig. 3A between iterations 3000 and 30,000. The straight line is a fit of the function $(R/S) = 1.35$ $(lag)^{0.54}$ to seven of the data points (filled squares) (13, 16). (**C**) Power-law scaling over three orders of magnitude of a simulated (open squares) and a real (filled squares) meandering river, the Juruá River (13). The scaling has been found by measuring the river with yardsticks of different lengths (the divider method) (15). The straight lines are fits of the function $N = ar^{-D}$ to the data, with $D = 1.18$ for the river and $D = 1.28$ for the simulation. The difference in the constant term is due to the different length of the river segments.
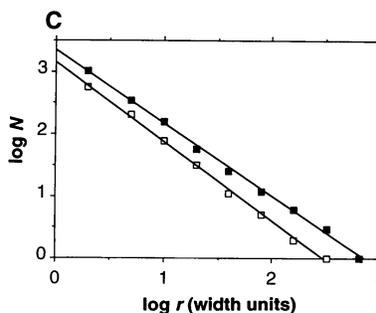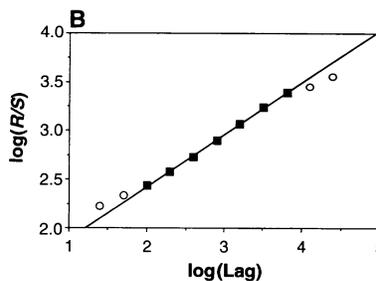
proximations to conditions that allow meandering channels in nature to develop sinuosities within the range found in simulations [see, for instance, (18) and (3)]. Howard's simulator uses a convolution integral to describe the memory effect of upstream meanders on migration rate at any given site along the river (7). It represents the river as a one-dimensional series of points along the river midline. For each iteration, the position of each point is recalculated starting at the upstream end, which is fixed. The points are moved according to the rate of laterally directed bank erosion in each point. The local rate of migration is assumed to be proportional to the curvature-dependent deviation of the thalweg path from the channel center line, measured as a near-bank velocity perturbation, $u_{c,x}$, which is described in the form of a convolution integral {see Parker and Andrews (8); D. Furbish [*J. Geol.* **16**, 752 (1988)], and D. Furbish [see (4)]}:

$$u_{c,x} = mC_{w,x} + n\int_A^x e^{-\beta x'} C_{w,x-x'} dx'$$

The integral describes the cumulative upstream effect of centrifugal forces and shoaling of flow over the point bar. $C_{w,x}$ is dimensionless channel center-line curvature, m, n, and β are constants, and x' is distance upstream from any given point x. A is a cutoff indicating the range of effective memory (the memory is nominally infinite, but in practice distinguishable information is not carried more than three to five bends downstream). The cutoff process is representative in the model by a simple decision rule, whereby any two non-neighbor points along the river cause the segment between them to be cut off if they are closer to each other than a set distance between one and two width units. In the simulations, I used a value of 0.3 for the input parameter k (nominal erosion rate), 0.01 for the bank resistance factor R, 0.5 for the Froude number F, and 0.2 for b (a measure of regional gradient that varies between 0 and 1).

9. A. Einstein, *Die Naturwissenschaften* **12**, 223 (1926); A. J. Odgaard, *Water Resour. Res.* **23**, 1225 (1987); M. A. Falcon Ascanio and J. F. Kennedy, *J. Fluid Mech.* **133**, 1 (1983).
10. J. M. Hooke, *Geomorphology* **14**, 235 (1995); J. Brice, *Geol. Soc. Am. Bull.* **85**, 581 (1974); S. M. Gagliano and P. C. Howard, in *River Meandering*, C. M. Elliott, Ed. (American Society of Civil Engineers, New York, 1984), pp. 147–158; G. W. Lewis and J. Lewin, *Spec. Publ. Int. Assoc. Sedimentol.* **6**, 145 (1983); J. M. Hooke and C. E. Redmond, in *Dynamics of Gravel Bed Rivers*, P. Billi *et al.*, Eds. (Wiley, Chichester, UK, 1992), pp. 549–563.
11. K. Hasegawa, in *River Meandering*, S. Ikeda and G. Parker, Eds. (American Geophysical Union, Water Research Monograph, vol. 12, Washington, DC, 1989), pp. 215–235.
12. H. Chaté, *Nonlinearity* **7**, 185 (1994); _____ and P. Manneville, *Physica D* **32**, 409 (1988).
13. A mean sinuosity of ≈3.14 is independent of b, R, and F over most of the range of these parameters (8). Also, simulations with rivers of different length showed that the standard deviation is an inverse function of the length of the river, whereas the mean is length-independent. The length dependence of sinuosity variance has no bearing on the scaling relations shown in Fig. 4, B and C, as both the magnitude of the scaling range and the fractal dimension are invariant with respect to river length (the variance dependence affects only the position of the scaling interval).
14. Consider the river fractal geometry idealized in the form of a perfectly symmetrical hierarchy of bends (with increasing wavelength) that are all cuts of a circle. Represent the actual planform as an initially straight line ($s = 1$), which is then superimposed on the undulations of bends. Each hierarchical level n contributes a component $s_n - 1$ to the sinuosity of the structure. At the smallest level, $n = 1$, the bends may be represented on the average as semicircles, so that $s_1 - 1 = \pi/2 - 1 \approx 0.5715$. The total sinuosity is

$$s = 1 + \sum_n (s_n - 1)$$

The average circle cuts at each level have been

found empirically for the simulation and the Juruá River (3). The amplitude at each level is close to 1/2, 1/2, 5/12, 4/12, 3/12, 2/12, and 1/12 times the circle section length, respectively. If we use these values, sinuosity measurements at each level yield $s \approx 1 + 0.5715 + 0.5715 + 0.440 + 0.280 + 0.172 + 0.0865 + 0.020 \approx 3.1415$.

15. If it is assumed that the river deposits sediment with a constant rate, then oxbow lakes are distributed in three dimensions purely according to the meander dynamics. Clustering then requires a threshold of areal closeness and a threshold of depth closeness. A range of possible threshold values is defined by the largest values that yield no clustering and the smallest values that generate one single, large cluster of all the oxbow lakes. Within this range, all threshold values generate power-law size-frequency distributions of one to two orders of magnitude (this scale-range appears to be limited by the finite size of the simulation).
16. B. B. Mandelbrot and J. R. Wallis, *Water Resour. Res.* **4**, 909 (1968); J. Feder, *Fractals* (Plenum, New York, 1988). Calculate for each iteration the accumulated departure of the sinuosity from the mean. For this derived time series, the range R is the difference between the average maximum value and the average minimum value for all possible segments of a given length. This range is normalized by dividing by S, which is the standard deviation of the mean sinuosity for the whole time series. Then R/S is scaled against the segment length or lag. A power-law interval indicates temporal scaling of the original sinuosity time series. The exponent is known as the Hurst exponent and is a measure of persistence of trends. A Hurst exponent of $H = 0.54$ reflects the appearance of "white noise" generated by chaos due to weak information-storage capacity and is observed as an absence of long-range correlations in time or space.
17. The fractal dimension, D, for the river planform as a whole is given by $N = ar^{-D}$, where r is the length of a yardstick in units of average river width and N is the number of yardsticks necessary to cover the river; a is a proportionality constant.
18. V. R. Baker, in *Fluvial Sedimentology*, A. D. Miall, Ed. (Canadian Society of Petroleum Geologists, Memoir vol. 5, Calgary, 1978), pp. 211–230.
19. Heraclitus, *On Nature* [fragments translated by P. Wheelwright, *Heraclitus* (Princeton Univ. Press, Princeton, NJ, 1959)]; G. S. Kirk, *Heraclitus, The Cosmic Fragments* (Cambridge Univ. Press, Cambridge, 1952); F. Nietzsche, *The Will to Power* [Random House (Vintage Books), New York, 1967]; G. Deleuze, *Nietzsche and Philosophy* (Athlone Press, London, 1983), pp. 47–49.
20. I thank A. Howard for generously making his simulator available for this study. I am grateful to P. Español for contributions to an earlier version of this report and for discussions. P. Bak, P. F. Friend, K. Richards, G. Stephens, and P. Charity suggested many improvements. L. Rush wrote the analysis programs. This research was supported by British Gas plc, Oryx (UK) Energy plc, Department of Trade and Industry (DTI), the Norwegian Research Council (NFR), and the British Council.

13 September 1995; accepted 3 January 1996

High-Temperature Study of Octahedral Cation Exchange in Olivine by Neutron Powder Diffraction

C. M. B. Henderson,* K. S. Knight, S. A. T. Redfern, B. J. Wood

Time-of-flight, neutron powder diffraction to 1000°C provides precise octahedral site occupancies and intersite distribution coefficients for $MnMgSiO_4$ and $MnFeSiO_4$ olivines. Intersite exchange occurs in minutes down to 500°C. Equilibrium distribution coefficients show that manganese ordering into the larger octahedral site decreases with increasing temperature. Exchange energies are 15.7 and 10.1 kilojoules per mole for magnesium-manganese and iron-manganese, respectively. Distribution coefficients deduced for $FeMgSiO_4$ olivine suggest an exchange energy of 4.8 kilojoules per mole. Intersite exchange energies are consistent with diffusion coefficients in the order iron > magnesium > manganese. Geothermometry based on magnesium-manganese and iron-manganese exchange may be possible only for samples equilibrated below 500°C.

As olivine [$(Mg,Fe,Mn)_2SiO_4$] is the major constituent of the Earth's upper mantle, its physical properties dominate the deep Earth's geophysical and geochemical properties down to the 410-km seismic discontinuity, which is attributed to the transitions of olivine to β- and γ-spinel-type polymorphs. A common simplifying assumption is that olivine is near ideal, with Mg and Fe fully disordered over M1

and M2, the two octahedral sites. Intracrystalline M-site partitioning would, however, be expected to modify olivine's thermodynamic stability, the diffusion rates of M-site metals, and (potentially) its elastic parameters. Furthermore, if significant partitioning does occur, M-site occupancies might also provide a means of using olivine as a petrogenetic indicator for thermometry and speedometry in a wide range of rocks.

Crystal chemical studies of olivines, primarily at room temperature (T) and pressure (P), show that divalent cations tend to order preferentially between M2, the larger site, and M1, the more distorted site; for example, Fe, Ni, and Zn into M1, and Mn and Ca into M2 (1). Early at-

C. M. B. Henderson, Department of Earth Sciences, University of Manchester, Manchester M13 9PL, UK.
K. S. Knight, ISIS, Rutherford Appleton Laboratory, Oxon OX11 0QX, UK.
S. A. T. Redfern, Department of Earth Sciences, University of Cambridge, Cambridge CB2 3EQ, UK.
B. J. Wood, Department of Geology, University of Bristol, Bristol BS8 1RJ, UK.

*To whom correspondence should be addressed.